International Journal of Solids and Structures 340 (2026) 114210

Contents lists available at ScienceDirect

International Journal of Solids and Structures

journal homepage: www.elsevier.com/locate/ijsolstr

Physical implications of decoupled boundary conditions in micropolar elasticity

Lucca Schek [a,*], Wolfgang H. Müller [a], Elena N. Vilchevskaya [a], Victor A. Eremeyev [b]

[a] Continuum Mechanics and Constitutive Theory, Institute of Mechanics, Technische Universität Berlin, Berlin, Germany

[b] Department of Civil and Environmental Engineering and Architecture (DICAAR), University of Cagliari, Cagliari, Italy

ARTICLE INFO

Keywords:
Micropolar elasticity
Cosserat continuum
Size effect
Nonclassical boundary conditions

ABSTRACT

The physical implications of boundary conditions in linearized micropolar elasticity are analyzed analytically and numerically. Firstly, a closed-form solution for the shearing of a block under arbitrary surface tractions, surface couple stresses, and volume loads is derived. This solution reveals the distinct physical roles of forces and couples, where forces primarily drive the displacement field and couples primarily drive the microrotation field, with the coupling parameter N controlling the strength of their interaction. Secondly, the torsion of a circular cylinder is analyzed, it is shown that the standard analytical solution implicitly couples a part of the microrotation to the macrorotation, which restricts the polar ratio to $\psi = 3/2$ for the ratio of micropolar to classical torsional rigidity to remain bounded as the cylinder diameter tends to zero. With numerical experiments it is demonstrated that this restriction is lifted when using decoupled micro-boundary conditions, and a pronounced size effect in torsional rigidity is recovered for the full admissible range $\psi \in (0, 3/2)$, suggesting that the conventional identification of $\psi = 3/2$ is a consequence of the boundary condition prescription rather than an intrinsic material property.

1. Introduction

The micropolar continuum theory extends the classical continuum with additional rotational degrees of freedom. This theory has its origins in the work by the Cosserat brothers from 1909 (Cosserat and Cosserat, 1909). A modern formulation in terms of explicit field equations and constitutive structure was introduced by Eringen in 1965 (Eringen, 1965), with comprehensive treatments and more widely used formulations available in Eringen (1999), Eremeyev et al. (2013), Ghiba et al. (2023). The framework has found application across a broad range of problems, including modeling size effects in bone material (Yang and Lakes, 1982; Park and Lakes, 1986) and foams (Lakes, 1983, 1986; Rueger and Lakes, 2016, 2019), homogenized description of metamaterials and structured media (Ha et al., 2016; Eremeyev and Reccia, 2022; Thiesen et al., 2026; Thatipelli et al., 2026), and mixed-dimensional formulations (Sky et al., 2024). Numerical implementations have been developed for both the nonlinear theory (Bauer et al., 2012; Erdelj et al., 2020, 2024) and the physically linear setting (Grbčić et al., 2018; Suh and Sun, 2019).

Physically, the micropolar description can be understood as a continuum description in which every material point has not only the ability to translate, but also to rotate (Schek et al., 2026). While the translation is understood as the observable deformation of the volume on the macro-scale, the rotation has the physical meaning of microrotation, which is not directly observable. For classical Cauchy continua, the concept of translational degrees of freedom is well understood and accepted to be observable, as are the concepts of stresses and strains. The same holds true for the translational degrees of freedom in a micropolar description, where they retain their physical meaning. However, the physical meaning of the rotational field and accompanying stresses as well as boundary conditions is not as clear. While the stress boundary conditions in a micropolar continuum, including tractions and couple moments, along with the volume loads, again including classical forces and couple moments, are well understood in an abstract sense and can be prescribed in a micropolar framework, their practical interpretation for a physical object remains ambiguous. The question of appropriate boundary conditions in micropolar elasticity has been discussed from various perspectives, including non-holonomic kinematic conditions relating virtual displacements and rotations at the boundary (Eremeyev, 2019).

The ambiguity becomes particularly evident in existing analytical solutions, such as those presented in Gauthier and Jahsman (1975), Park and Lakes (1987), where the macrorotation induced by the displacement field and the microrotation of a material point are not

* Corresponding author.
E-mail address: l.schek@tu-berlin.de (L. Schek).

https://doi.org/10.1016/j.ijsolstr.2026.114210
Received 7 February 2025; Received in revised form 10 May 2026; Accepted 8 July 2026
Available online 16 July 2026

explicitly distinguished fully. This approach is more in line with couple stress theory, where the microrotation is strongly coupled to the macrorotation. In these analytical solutions, derived for the cylindrical bending of a plate and the pure torsion of a circular cylinder, the forces and couple moments are chosen such that micro- and macro-rotations coincide at the boundary, producing a specific deformation state. These solutions have been used to identify Cosserat material parameters from size-effect experiments in the above-mentioned studies. What stands out is that in all of these identifications, one of the micropolar material parameters, the polar ratio ψ, is consistently found to be $3/2$, see *e.g.* Tab. 1 in Lakes (1995). This parameter choice renders the curvature energy not pointwise positive definite, yet it is a necessity under the boundary conditions of Gauthier and Jahsman (1975) as this is the only value for which the ratio of micropolar to classical torsional rigidity remains bounded as the specimen diameter tends to zero (Neff, 2006; Neff and Jeong, 2009; Neff et al., 2010). While energetically admissible, other values of $\psi \in (0, 3/2)$ yield an unbounded ratio of micropolar to classical torsional rigidity as the diameter of the torsion rod tends to zero. The present work shows numerically that this restriction on ψ is a consequence of the boundary condition prescription rather than a material requirement.

In contrast to available analytical solutions, in this work an analytical solution for the shearing of a long block is derived, which does not start from a predetermined deformation shape. Instead, the solution is found for arbitrary but constant loading conditions at both the surface and in the volume, employing a reduced one-dimensional *ansatz*. In this way, the effects of surface tractions and surface couple stresses on the displacement and microrotation fields can be traced independently, providing a physical understanding of the micropolar boundary conditions that goes beyond simple stiffening effects (Schek and Müller, 2026). In particular, this solution demonstrates that forces and couples drive the displacement and microrotation fields independently when the micro-boundary condition is not constrained to follow the macrorotation.

Building on this understanding, the torsion of a circular cylinder is revisited numerically. The torsional rigidity, which exhibits a pronounced size effect in the analytical solution of Gauthier and Jahsman (1975), is studied here for boundary conditions applied separately to the macrorotation and microrotation fields. It is shown that a measurable size effect and a bounded torsional rigidity ratio are retained for the full admissible range $\psi \in (0, 3/2)$ when the microrotation is left free at the boundary. As a demonstration, the polar ratio is identified from the torsion size effect data of Rueger and Lakes (2019) using decoupled boundary conditions, yielding a value $\psi < 3/2$ with bounded stiffness and comparable fit quality to the coupled analytical solution. Numerical solutions are obtained using the finite element software NGSolve[1] (Schöberl, 1997, 2014) and are available online.[2]

This paper is structured as follows. In Section 2, the linearized micropolar framework is briefly outlined, and the constitutive equations are presented in the parameter sets most commonly used in the literature. In Section 3, the analytical solution for the shearing of a micropolar block is derived and discussed. In Section 4, the torsion of a circular cylinder is studied numerically, and the torsional rigidity is compared to the analytical solution of Gauthier and Jahsman (1975) for both coupled and decoupled micro-boundary conditions.

2. Linear micropolar isotropic solids

In this section, the linearized micropolar theory is outlined. Throughout this work, right gradients $\mathrm{grad}(\boldsymbol{u}) = \boldsymbol{u} \otimes \nabla = \nabla \boldsymbol{u}$, or fully in index notation $\frac{\partial u_i}{\partial x_j} = u_{i,j}$, are used. This is in contrast to the literature by Eringen, where left gradients are employed. While full tensor notation is primarily used, index notation employing Einstein's summation convention is provided alongside for equations relevant to the reproduction of analytical and numerical results.

2.1. Kinematics and strain measures

The micropolar continuum, depicted in Fig. 1, can be understood as an enriched Cauchy continuum in which every material point possesses not only a translational displacement $\boldsymbol{u}$ but also an independent microrotation $\boldsymbol{\theta}$ as a separate degree of freedom. This microrotation $\boldsymbol{\theta}$ describes the change in orientation of a material point between the reference and deformed configuration. The linearized strain measures of the micropolar continuum are obtained by linearizing the Biot-like Cosserat strain tensor of the finite deformation theory (Pietraszkiewicz and Eremeyev, 2009). For small displacements and rotations, these reduce to the non-symmetric strain tensor

$$\boldsymbol{\varepsilon} = \mathrm{grad}(\boldsymbol{u}) - \boldsymbol{1} \times \boldsymbol{\theta} \quad \Leftrightarrow \quad \varepsilon_{ij} = u_{i,j} + \epsilon_{ijk}\theta_k, \tag{1}$$

and the wryness tensor

$$\boldsymbol{\varkappa} = \mathrm{grad}(\boldsymbol{\theta}) \quad \Leftrightarrow \quad \varkappa_{ij} = \theta_{i,j}, \tag{2}$$

where ϵ_{ijk} are the components of the permutation tensor and the cross product $\times$ is defined as in Eremeyev et al. (2013, p. 86). When the microrotation coincides with the macrorotation, $\theta_i = \frac{1}{2}\epsilon_{ijk}u_{k,j}$, the linearized strain (1) reduces to the symmetric engineering strain $\varepsilon_{ij} = \frac{1}{2}(u_{i,j} + u_{j,i})$ of classical elasticity.

2.2. Balance equations

In the simplest form of a micropolar continuum, where the specific momentum is recognized as the velocity $\boldsymbol{v} = \dot{\boldsymbol{u}}$, the local balance of linear momentum is given by

$$\begin{aligned} \rho\frac{\mathrm{d}\boldsymbol{v}}{\mathrm{d}t} &= \mathrm{div}(\boldsymbol{\sigma}) + \rho\boldsymbol{f} \quad &\Leftrightarrow \quad \rho\frac{\mathrm{d}v_i}{\mathrm{d}t} &= \sigma_{ij,j} + \rho f_i, \qquad &\boldsymbol{x} \in \Omega \\ \boldsymbol{t}^{\mathrm{s}} &= \boldsymbol{\sigma}\cdot\boldsymbol{n} \quad &\Leftrightarrow \quad t_i^{\mathrm{s}} &= \sigma_{ij}n_j, \qquad &\boldsymbol{x} \in \partial\Omega \end{aligned} \tag{3}$$

where $\boldsymbol{f}$ represents the volume force (force per unit mass), ρ is the density (mass per unit volume), $\boldsymbol{\sigma}$ is the Cauchy stress tensor and $\boldsymbol{t}^{\mathrm{s}}$ is the surface traction (force per unit area), see Fig. 1. Notably, the balance of linear momentum in a micropolar continuum is identical with that in a classical continuum.[3] However, the inclusion of rotational degrees of freedom necessitates a more generalized form of the angular momentum balance. Unlike in a classical continuum, where the balance of angular momentum is derived purely as a consequence of the linear momentum balance (referred to as the specific moment of momentum, $\boldsymbol{x} \times \boldsymbol{v}$), a micropolar description requires the recognition that the total angular momentum must consist of the moment of momentum $\boldsymbol{x}\times\boldsymbol{v}$ and a dynamic spin $\boldsymbol{s}$, which can be understood as the angular momentum due to the rotation of a material point with angular velocity $\boldsymbol{\omega} = \dot{\boldsymbol{\theta}}$

$$\boldsymbol{s} = \boldsymbol{J}\cdot\boldsymbol{\omega}, \tag{4}$$

where $\boldsymbol{J}$ is the microinertia tensor of a material point, directly corresponding in its meaning to the inertia tensor in rigid body mechanics. It should be noted that more general forms of (4) exist, see Müller et al. (2020), Eremeyev and Reccia (2022). With that, the total balance of angular momentum then is

$$\rho\frac{\mathrm{d}}{\mathrm{d}t}(\boldsymbol{x}\times\boldsymbol{v} + \boldsymbol{s}) = \mathrm{div}(\boldsymbol{x}\times\boldsymbol{\sigma} + \boldsymbol{\mu}) + \rho(\boldsymbol{x}\times\boldsymbol{f} + \boldsymbol{m}), \tag{5}$$

where $\boldsymbol{x}\times\boldsymbol{f}$ expresses the torque exerted by volume forces, $\boldsymbol{m}$ are volume couples (torque per unit mass) directly acting on the rotation of material points, see Fig. 1, and $\boldsymbol{\mu}$ is the couple stress tensor. From (3) with $\frac{\mathrm{d}}{\mathrm{d}t}(\boldsymbol{x}\times\boldsymbol{v})$ and (5) the balance of dynamic spin can be derived by subtracting the moment of momentum from the total angular momentum as

$$\begin{aligned} \rho\frac{\mathrm{d}\boldsymbol{s}}{\mathrm{d}t} &= \mathrm{div}(\boldsymbol{\mu}) - \boldsymbol{\sigma}_\times + \rho\boldsymbol{m} \quad &\Leftrightarrow \quad \rho\frac{\mathrm{d}s_i}{\mathrm{d}t} &= \mu_{ij,j} - \sigma_{jk}\epsilon_{jki} + \rho m_i, \qquad &\boldsymbol{x} \in \Omega \\ \boldsymbol{m}^{\mathrm{s}} &= \boldsymbol{\mu}\cdot\boldsymbol{n} \quad &\Leftrightarrow \quad m_i^{\mathrm{s}} &= \mu_{ij}n_j, \qquad &\boldsymbol{x} \in \partial\Omega \end{aligned}$$

[1] www.ngsolve.org
[2] www.github.com/lschek/micropolar_elasticity_ngsolve
[3] This does not hold universally, as formulations exist in which the specific momentum has a more general form, see Müller et al. (2020).

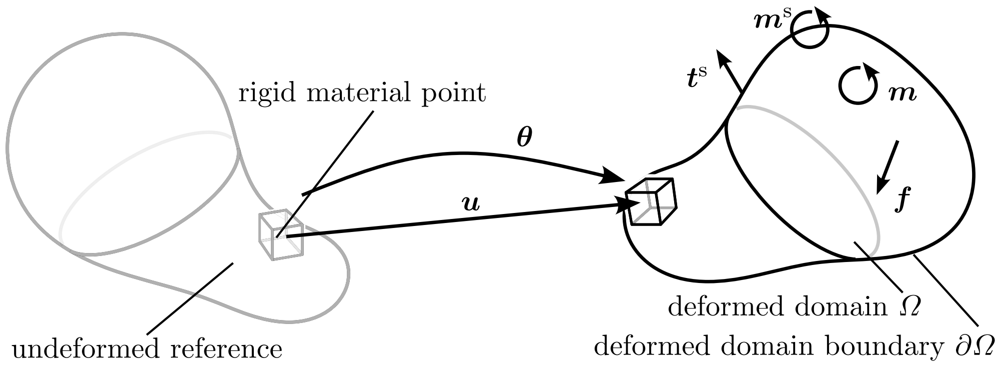

Fig. 1. Every rigid material point in a micropolar continuum description is assigned a rotational and translational degree of freedom. As a consequence of this enriched description, loading can appear via forces and couples on the surface $\boldsymbol{t}^{\mathrm{s}}$ and $\boldsymbol{m}^{\mathrm{s}}$ as well as in the volume $\boldsymbol{f}$ and $\boldsymbol{m}$.

(6)

with the Gibbsian cross $\boldsymbol{\sigma}_{\times}$ defining the vector invariant $\sigma_{ij}\boldsymbol{e}_i \times \boldsymbol{e}_j$. Here, the surface moment couples $\boldsymbol{m}^{\mathrm{s}}$ (torque per unit area) were introduced, see Fig. 1. The meaning of these balances has extensively been discussed in Müller et al. (2020), although for a formulation using left gradients in the balance equations.

The balance of virtual work coincides with the sum of the weak formulations of the balances for linear momentum and spin. To obtain these, the momentum balances (3) and (6) are multiplied by virtual- or test-functions and each is integrated over the domain Ω, which describes the volume of the micropolar solid. In the stationary case, the total virtual work is then obtained as

$$\begin{aligned}\int_{\Omega}\left[\boldsymbol{\sigma}\left(\boldsymbol{u},\boldsymbol{\theta}\right) : (\operatorname{grad}(\delta\boldsymbol{u}) - \boldsymbol{1}\times\delta\boldsymbol{\theta}) + \boldsymbol{\mu}\left(\boldsymbol{\theta}\right) : \operatorname{grad}(\delta\boldsymbol{\theta})\right]\,\mathrm{d}V\\ = \int_{\Omega}\left[\rho\boldsymbol{f}\cdot\delta\boldsymbol{u} + \rho\boldsymbol{m}\cdot\delta\boldsymbol{\theta}\right]\,\mathrm{d}V + \int_{\Gamma_{\mathrm{N}}}\left[\boldsymbol{t}^{\mathrm{s}}\cdot\delta\boldsymbol{u} + \boldsymbol{m}^{\mathrm{s}}\cdot\delta\boldsymbol{\theta}\right]\,\mathrm{d}A,\end{aligned}\tag{7}$$

or equivalently in index notation

$$\begin{aligned}\int_{\Omega}\left[\sigma_{ij}\left(\delta u_{i,j} + \varepsilon_{ijk}\delta\theta_k\right) + \mu_{ij}\delta\theta_{i,j}\right]\,\mathrm{d}V\\ = \int_{\Omega}\left[\rho f_i\delta u_i + \rho m_i\delta\theta_i\right]\,\mathrm{d}V + \int_{\Gamma_{\mathrm{N}}}\left[t_i^{\mathrm{s}}\delta u_i + m_i^{\mathrm{s}}\delta\theta_i\right]\,\mathrm{d}A.\end{aligned}\tag{8}$$

2.3. Constitutive equations

The constitutive equations for an isotropic linear micropolar solid express the stress and couple stress as

$$\sigma_{ij} = \lambda\varepsilon_{pp}\delta_{ij} + (\mu+\mu_{\mathrm{c}})\varepsilon_{ij} + (\mu-\mu_{\mathrm{c}})\varepsilon_{ji},\tag{9}$$

$$\mu_{ij} = \alpha\theta_{p,p}\delta_{ij} + (\beta+\gamma)\theta_{i,j} + (\beta-\gamma)\theta_{j,i},\tag{10}$$

following Nowacki (1986) as adopted in Grbčić et al. (2018). This parameterization has the advantage of cleanly separating the classical Lamé constants λ and μ from the micropolar constants μ_{c}, α, β, γ, avoiding the entanglement present in Eringen's original notation (Eringen, 1965; Hassanpour and Heppler, 2017), see also Appendix A. A full conversion between the three parameter sets most commonly used in the literature is given in Table 1. The table also includes a third set of elastic parameters. Unlike the constants presented so far, this third set carries a unique physical significance for each parameter. These parameters were introduced by Gauthier and Jahsman in Gauthier and Jahsman (1975) and have the advantage of being directly measurable in experiments, *e.g.*, Lakes (1983, 1991), Park and Lakes (1986). The so-called engineering parameters include the classical shear modulus $G = \mu$ and Poisson's ratio ν, which retain the same meaning as in classical elasticity theory, as well as four additional micropolar parameters. Within the micropolar engineering parameters, two characteristic length scales are introduced: one for torsion, ℓ_{t}, and one for bending, ℓ_{b}. These lengths arise in analytical solutions to pure bending and torsion problems, as derived in Gauthier and Jahsman (1975), and represent physical length scales that directly influence microstructural behavior, which classical elasticity cannot capture. Furthermore, the coupling number $N \in (0,1)$ is introduced to describe the strength of coupling between micro- and macrorotation. The limit $N \to 1$ describes a fully coupled micro- and macrorotation and the limit $N \to 0$ describes a fully decoupled micro- and macrorotation. The last parameter is the polar ratio $\psi \in (0, 3/2)$, which characterizes the rotation sensitivity (Lakes, 2016; Beveridge et al., 2013). A full conversion guide for this set of experimentally measurable parameters to the parameters used in the constitutive modeling is also provided in Table 1. Young's modulus E as a third classically measurable parameter can be obtained as usual from G and ν

$$E = 2G(1+\nu) = \frac{\mu\left(3\lambda+2\mu\right)}{\lambda+\mu} = \frac{\left(\tilde{\kappa}+2\tilde{\mu}\right)\left(3\tilde{\lambda}+2\tilde{\mu}+\tilde{\kappa}\right)}{2\tilde{\lambda}+2\tilde{\mu}+\tilde{\kappa}}.\tag{11}$$

3. Shear of a rectangular block

In this section, the situation as depicted in Fig. 2 is studied. A rectangular block consisting of a micropolar material is subjected to external volume forces and couples

$$\boldsymbol{f} = f_x\boldsymbol{e}_x, \quad \boldsymbol{m} = m_z\boldsymbol{e}_z,\tag{12}$$

pulling the material in the positive $\boldsymbol{e}_x$ direction on the one hand and twisting it positively around the $\boldsymbol{e}_z$ direction on the other. Additionally, the block is subjected to surface tractions $\boldsymbol{t}^{\mathrm{s}}$ and couples $\boldsymbol{m}^{\mathrm{s}}$ on the boundary surface at $y = h$

$$\boldsymbol{t}^{\mathrm{s}} = t_x^{\mathrm{s}}\boldsymbol{e}_x, \quad \boldsymbol{m}^{\mathrm{s}} = m_z^{\mathrm{s}}\boldsymbol{e}_z,\tag{13}$$

with $\boldsymbol{t}^{\mathrm{s}}$ resembling the boundary conditions of the classical shearing problem. The derivation of the solution to this problem in micropolar elasticity, although in absence of surface tractions and surface moment couples, was previously described in Müller and Vilchevskaya (2024, p. 199). The block is sufficiently extended in the $\boldsymbol{e}_x$ and $\boldsymbol{e}_z$ directions, such that following semi-inverse *ansatz* is justified

$$\boldsymbol{u} = u_x\left(y\right)\boldsymbol{e}_x, \quad \boldsymbol{\theta} = \theta_z\left(y\right)\boldsymbol{e}_z,\tag{14}$$

in which all components of displacement and microrotation vanish, except for the displacement in x-direction and microrotation around the z-axis. Inserted into the balance equations for linear momentum and dynamic spin, (3) and (6) this yields in following set of partial differential equations

$$\left(\mu+\mu_{\mathrm{c}}\right)\frac{\partial^2 u_x}{\partial y^2} + 2\mu_{\mathrm{c}}\frac{\partial\theta_z}{\partial y} + \rho f_x = 0,\tag{15}$$

$$(\beta+\gamma)\frac{\partial^2\theta_z}{\partial y^2} - 4\mu_{\mathrm{c}}\left(\theta_z + \frac{1}{2}\frac{\partial u_x}{\partial y}\right) + \rho m_z = 0,\tag{16}$$

Table 1
Conversion of elastic parameters in micropolar elasticity.

	Eringen (1999) $\tilde{\lambda}, \tilde{\mu}, \tilde{\kappa}, \tilde{\alpha}, \tilde{\beta}, \tilde{\gamma}$	Grbčić et al. (2018) $\lambda, \mu, \mu_c, \alpha, \beta, \gamma$	Engineering (Lakes, 2016) $G, \nu, \ell_t, \ell_b, N, \psi$
$\tilde{\lambda}, \tilde{\mu}, \tilde{\kappa}, \tilde{\alpha}, \tilde{\beta}, \tilde{\gamma}$	–	$\lambda = \tilde{\lambda},\ \mu = \frac{1}{2}\tilde{\kappa} + \tilde{\mu}$, $\mu_c = \frac{\tilde{\kappa}}{2}, \quad \alpha = \tilde{\alpha}$, $\beta = \frac{1}{2}(\tilde{\gamma} + \tilde{\beta})$, $\gamma = \frac{1}{2}(\tilde{\gamma} - \tilde{\beta})$	$G = \frac{1}{2}\tilde{\kappa} + \tilde{\mu},\ \nu = \frac{\tilde{\lambda}}{\tilde{\kappa}+2\tilde{\lambda}+2\tilde{\mu}}$ $\ell_t = \sqrt{\frac{\tilde{\beta}+\tilde{\gamma}}{\tilde{\kappa}+2\tilde{\mu}}},\ \ell_b = \sqrt{\frac{1}{2}\frac{\tilde{\gamma}}{\tilde{\kappa}+2\tilde{\mu}}}$ $N^2 = \frac{\tilde{\kappa}}{2(\tilde{\mu}+\tilde{\kappa})},\ \psi = \frac{\tilde{\beta}+\tilde{\gamma}}{\tilde{\alpha}+\tilde{\beta}+\tilde{\gamma}}$
$\lambda, \mu, \mu_c, \alpha, \beta, \gamma$	$\tilde{\lambda} = \lambda,\ \tilde{\mu} = \mu - \mu_c$, $\tilde{\kappa} = 2\mu_c, \quad \tilde{\alpha} = \alpha$, $\tilde{\beta} = \beta - \gamma,\ \tilde{\gamma} = \beta + \gamma$	–	$G = \mu,\ \nu = \frac{\lambda}{2(\lambda+\mu)}$ $\ell_t = \sqrt{\frac{\beta}{\mu}},\ \ell_b = \frac{1}{2}\sqrt{\frac{\beta+\gamma}{\mu}}$, $N^2 = \frac{\mu_c}{\mu_c+\mu},\ \psi = \frac{2\beta}{\alpha+2\beta}$
$G, \nu, \ell_t, \ell_b, N, \psi$	$\tilde{\lambda} = \frac{2\nu G}{1-2\nu},\ \tilde{\mu} = \frac{G(1-2N^2)}{1-N^2}$, $\tilde{\kappa} = \frac{2GN^2}{1-N^2},\ \tilde{\alpha} = \frac{2G\ell_t^2(1-\psi)}{\psi}$, $\tilde{\beta} = 2G\left(\ell_t^2 - 2\ell_b^2\right)$, $\tilde{\gamma} = 4G\ell_b^2$	$\lambda = \frac{2\nu G}{1-2\nu},\ \mu = G$, $\mu_c = \frac{GN^2}{1-N^2}$, $\alpha = \frac{2G\ell_t^2(1-\psi)}{\psi}$, $\beta = G\ell_t^2$, $\gamma = G\left(4\ell_b^2 - \ell_t^2\right)$	–

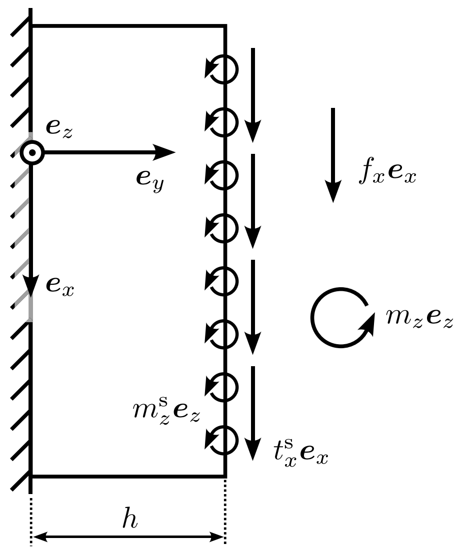

Fig. 2. Shearing of a block under gravity and a volumetric couple moment field. The block is assumed infinite in the x and z directions.

which, except for the inhomogeneous contribution of volume forces and couples, coincides mathematically with the structure of the boundary value problem for a micropolar fluid investigated in Rickert et al. (2019). The block is fixed on the wall and the essential Dirichlet boundary conditions are

$$u_x\,(y = 0) = 0, \quad \theta_z\,(y = 0) = 0, \tag{17}$$

meaning that both displacement and microrotation are prohibited at the left boundary. Furthermore, the surface at $y = h$ brings with it the natural inhomogeneous Neumann boundary conditions from (3) with $\boldsymbol{n} = \boldsymbol{e}_y$

$$\begin{aligned} \sigma_{xy}(y = h) &= 2\mu_c\theta_z(y = h) + \left(\mu_c + \mu\right)\left.\frac{\mathrm{d}u_x}{\mathrm{d}y}\right|_{y=h} = t_x^s, \\ \mu_{zy}(y = h) &= (\beta + \gamma)\left.\frac{\mathrm{d}\theta_z}{\mathrm{d}y}\right|_{y=h} = m_z^s\,. \end{aligned} \tag{18}$$

The solution to this system of ODEs is found via formulation of a particular and homogeneous solution,

$$u_x(y) = u_x^p(y) + u_x^h(y), \quad \theta_z(y) = \theta_z^p(y) + \theta_z^h(y)\,, \tag{19}$$

of which the homogeneous solution can be taken from Rickert et al. (2019) where it was derived for a stationary micropolar fluid

$$u_x^{\text{hom}}(y) = c_1 + c_2 y - c_3 N 2\ell_b \exp\left(N\frac{y}{\ell_b}\right) + c_4 N 2\ell_b \exp\left(-N\frac{y}{\ell_b}\right), \tag{20}$$

$$\theta_z^{\text{hom}}(y) = -\frac{1}{2}c_2 + c_3 \exp\left(N\frac{y}{\ell_b}\right) + c_4 \exp\left(-N\frac{y}{\ell_b}\right), \tag{21}$$

with the coupling number N and characteristic length of bending ℓ_b as were introduced in Table 1. The constants c_i are to be determined from the boundary conditions (17) and (18). The particular solution satisfying the inhomogeneous set of ODEs is found from a polynomial ansatz as

$$u_x^p(y) = -\frac{\rho f_x}{2\mu}y^2, \quad \theta_z^p(y) = \frac{\rho}{4}\left(\frac{2f_x}{\mu}y + \frac{m_z}{\mu_c}\right). \tag{22}$$

From the boundary conditions (17) and (18), the constants for the homogeneous solution in (20) can be determined as

$$\begin{aligned} c_1 &= \frac{N\left(m_z^s - 2f_x\ell_b^2\rho\right)\frac{1}{\cosh(hN/\ell_b)} + \ell_b\tanh\left(\frac{hN}{\ell_b}\right)\left(m_z\rho - 2N^2(f_x h\rho + t_x^s)\right)}{2\mu N}, \\ c_2 &= \frac{2f_x h\rho - m_z\rho + 2t_x^s}{2\mu}, \\ c_3 &= \frac{N\exp\left(\frac{hN}{\ell_b}\right)\left(m_z^s - 2f_x\ell_b^2\rho\right) + \ell_b\left(2N^2(f_x h\rho + t_x^s) - m_z\rho\right)}{4\mu\ell_b N^2\left(\exp\left(\frac{2hN}{\ell_b}\right) + 1\right)}, \\ c_4 &= \frac{\exp\left(\frac{hN}{\ell_b}\right)\left(\ell_b\left(\exp\left(\frac{hN}{\ell_b}\right)\left(2N^2(f_x h\rho + t_x^s) - m_z\rho\right) + 2f_x\ell_b N\rho\right) - m_z^s N\right)}{4\mu\ell_b N^2\left(\exp\left(\frac{2hN}{\ell_b}\right) + 1\right)}, \end{aligned} \tag{23}$$

with which the analytical solution to the volume and surface induced shearing problem is now fully defined. It should be noted that by setting the volume entities f_x and m_z to zero, the micropolar equivalent to the classical shearing problem with added surface couples can be obtained. Similarly, the analytical solution to a micropolar block with fixed microrotation at the base under purely classical surface traction t_x^s is obtained when additionally setting m_z^s to zero.

3.1. Limit cases for the micropolar parameters

The rather lengthy solution obtained from the constants (23) can be investigated for limiting cases in the characteristic length ℓ_b and the coupling number N. Starting first with the coupling number, the solution for the displacement

$$\lim_{N\to 0} u_x(y) = \frac{t_x^s y}{\mu} + \frac{\rho f_x(2h - y)y}{2\mu} \tag{24}$$

reduces to that of the classical shearing problem, and the couples m_z^s and m_z have no effect on the displacement. The microrotation

$$\lim_{N\to 0} \theta_z(y) = \frac{m_z^s y}{4\mu\ell_b^2} + \frac{\rho m_z(2h - y)y}{8\mu\ell_b^2} \tag{25}$$

on the other hand is now purely affected by the couple, with no influence from the traction t_x^s and volume force f_x. This shows that the microrotation and macrodisplacement are fully decoupled when N vanishes. In the limit $N \to 1$, corresponding to $\mu_c \gg \mu$, the micropolar coupling becomes infinitely stiff and the microrotation is constrained to follow the macrorotation everywhere in the domain

$$\lim_{N\to 1} \theta_z(y) = -\frac{1}{2}\frac{\partial u_x}{\partial y}\bigg|_{N=1}, \tag{26}$$

recovering couple stress theory, in which the microrotation is no longer an independent field but is tied to the displacement gradient. This limit is relevant for materials in which the microstructure is strongly constrained to follow the macroscopic deformation, such as graphite (Tang, 1983), where couple stress theory has been used to interpret size effects in bending. It should be noted that this couple stress recovery differentiates the present solution from the pure bending solution of Gauthier and Jahsman (1975), Grbčić et al. (2019), where N does not appear in the solution at all since the boundary conditions enforce micro- and macrorotation to coincide throughout the domain.

From the microrotation (25) in the fully decoupled material ($N \to 0$), the meaning of the characteristic length of bending ℓ_b can also be understood. Here, while the fully decoupled displacement field would not be affected, the rotation would vanish when this length is significantly large compared with the size of the block, and one would end up with the purely classical solution in which no microrotation exists. This limiting case can also be analyzed more formally by looking at the solution as the characteristic length of bending approaches infinity. Then the displacement

$$\lim_{\ell_b\to\infty} u_x(y) = \left(1-N^2\right)\left(\frac{t_x^s y}{\mu} + \frac{\rho f_x(2h-y)y}{2\mu}\right) \tag{27}$$

is again purely produced by the surface traction and volume force while the couples have no effect. In a fully coupled formulation, with $N = 1$, this deformation would also vanish, and an infinite ℓ_b would express a rigid volume. The microrotation

$$\lim_{\ell_b\to\infty} \theta_z(y) = 0 \tag{28}$$

will vanish regardless of the value of N. The infinite characteristic length produces what can be understood as an underlying microstructure which is rigid with respect to rotation. Together, these limiting cases demonstrate how the coupling parameter N controls the interaction between the force-driven displacement field and the couple-driven microrotation field, while ℓ_b controls the stiffness of the microstructure against rotation.

A parameter study for the coupling number N is carried out in Fig. 3(a), with all volume loads and surface couples set to zero ($f_x = m_z = m_z^s = 0$) and parameters, $h = 1\,\mathrm{m}$, $\mu = 600\,\mathrm{N/m^2}$, $t_x^s = 100\,\mathrm{N/m^2}$ chosen for illustrative purposes. The characteristic length $\ell_b = 0.5h$ is chosen such that microstructural effects are easily visible. As N approaches zero, the displacement converges to the classical linear solution and the microrotation vanishes. In this case, the two fields are fully decoupled and the surface traction drives only the displacement. As N increases, the material stiffens and the displacement develops a nonlinear profile, while the microrotation grows in magnitude. As the coupling increases and N approaches one, both the maximum displacement is decreased and the maximum value of microrotation are significantly reduced compared to the displacement and the macrorotation of the classical solution $\frac{1}{2}\partial u_x^{cl}/\partial y = t_x^s/2\mu$. This is due to the strong effect of the boundary condition (17) for θ_z at $y = 0$ which forces a zero slope for the displacement when the coupling is large.

The effect of the characteristic length ℓ_b is shown in Fig. 3(b), with $N = 0.5$. For small ℓ_b, the displacement approaches the classical solution and the microrotation reaches the macrorotation of the classical solution as the microstructure is soft enough that it follows the macrorotation. As ℓ_b increases, the microstructure becomes progressively stiffer and the displacement is scaled toward $(1-N^2) = 0.75$ of the classical value, consistent with (27), and the microrotation vanishes, consistent with (28).

3.2. Numerical implementation

The derived analytical solution is used to validate a numerical finite element solution obtained with the open-source finite element library NGSolve (Schöberl, 1997, 2014). The weak formulation (8) is implemented directly in a mixed function space, where both $\boldsymbol{u}$ and $\boldsymbol{\theta}$ are approximated using second-order Lagrangian polynomials. The domain has an aspect ratio of 1×2 and is discretized with a uniform mesh. A plane strain formulation with $u_i = [u_x, u_y, 0]$ and $\theta_i = [0, 0, \theta_z]$ is used to enforce the assumption of independence of the solution in the z-direction, and periodic boundary conditions for both $\boldsymbol{u}$ and $\boldsymbol{\theta}$ are applied at the boundaries in the limits of x to enforce the assumption of independence in the x-direction. The surface and volume loads are set to $\rho f_x = 50\,\mathrm{N/m^3}$, $\rho m_z = 50\,\mathrm{Nm/m^3}$, $t_x^s = 50\,\mathrm{N/m^2}$ and $m_z^s = 50\,\mathrm{Nm/m^2}$ and the elastic material parameters are $\mu = 600\,\mathrm{N/m^2}$, $\ell_b = 0.1h$, $N = 0.5$. The remaining parameters, which are not affecting the analytical solution and do not have an influence on the solution are chosen as $\ell_t = 0.1h$, $\nu = 0.25$, $\psi = 0.5$. Starting from a coarse mesh of 4×8 elements, see Fig. 4(b), uniform refinement is performed up to a mesh size of $h_{\mathrm{mesh}} = 1/64h$. The relative errors are computed as

$$e_{\mathrm{rel},\boldsymbol{u}} = \frac{\|\boldsymbol{u}^{\mathrm{num}} - \boldsymbol{u}^{\mathrm{ana}}\|_{L^2}}{\|\boldsymbol{u}^{\mathrm{ana}}\|_{L^2}}, \quad e_{\mathrm{rel},\boldsymbol{\theta}} = \frac{\|\boldsymbol{\theta}^{\mathrm{num}} - \boldsymbol{\theta}^{\mathrm{ana}}\|_{L^2}}{\|\boldsymbol{\theta}^{\mathrm{ana}}\|_{L^2}}, \tag{29}$$

where $\boldsymbol{u}^{\mathrm{ana}} = u_x^{\mathrm{ana}}\boldsymbol{e}_x$ and $\boldsymbol{\theta}^{\mathrm{ana}} = \theta_z^{\mathrm{ana}}\boldsymbol{e}_z$ are the analytical solutions restricted to their nonzero components. Both fields converge at the expected rate of $\mathcal{O}(h_{\mathrm{mesh}}^3)$ for second-order Lagrangian polynomials.

4. Torsion of a circular cylinder

Motivated by the observation in Section 3 that forces and couples drive the two fields independently when the boundary conditions are unconstrained, it is analyzed what happens to the torsion problem when the same logic is applied to the rotating face. A fully closed-form analytical solution for the torsion of a circular cylinder was derived in Gauthier and Jahsman (1975). The problem is formulated here for a cylinder with diameter d which extends symmetrically around $z = 0$ along the z-axis with length $2L$, as depicted in Fig. 5.

In Gauthier and Jahsman (1975), the boundary conditions for this problem are chosen such that both tractions and couple moments contribute together

$$M_T = \int_{A|z=L} (r t_\varphi^s + m_z^s)\,\mathrm{d}A \tag{30}$$

with t_φ^s and m_z^s from Grbčić et al. (2018) given in Appendix B. This distribution of the total twisting moment is carefully chosen in order to assure a specific deformation which in cylindrical coordinates is

$$\boldsymbol{u} = \begin{pmatrix} 0 \\ \varphi\frac{z}{L}r \\ 0 \end{pmatrix} = \varphi\frac{z}{L}r\boldsymbol{e}_\varphi, \qquad \boldsymbol{\theta} = \begin{pmatrix} \phi(r) \\ 0 \\ \varphi\frac{z}{L} \end{pmatrix} = \phi(r)\boldsymbol{e}_r + \varphi\frac{z}{L}\boldsymbol{e}_z \tag{31}$$

with $\phi(r)$ and φ as given in Appendix B which is equivalent to the torsion presented in Ghiglione and Forest (2022). What immediately becomes noticeable is that the axial microrotation component $\theta_z = \varphi z/L$ coincides exactly with the macrorotation around the z-axis

$$\theta_z = \varphi\frac{z}{L} = \frac{1}{2r}\frac{\partial(r u_\varphi)}{\partial r}, \tag{32}$$

similar to a couple stress formulation. The radial component $\theta_r = \phi(r)$, however, is a genuinely micropolar quantity with no classical counterpart which is controlled by the coupling.

The treatment of microrotation boundary conditions warrants further discussion. While the displacement field corresponds to the observable deformation of the continuum, the microrotation field captures the rotation of the material's substructure, which is a quantity that

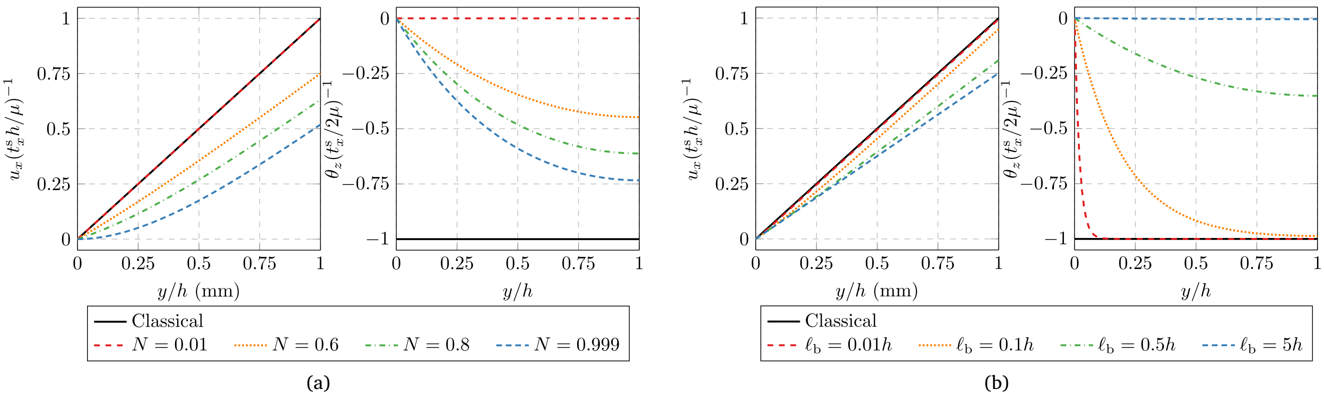

Fig. 3. Parameter study for (a) the coupling number N with $m_z^s = f_x = m_z = 0$ and $\ell_b = 0.5h$, and (b) the characteristic bending length ℓ_b with $N = 0.5$. The displacement is normalized by the classical solution $u_x^{cl}(h) = t_x^s h/\mu$ and microrotation by the classical macrorotation $t_x^s/(2\mu)$.

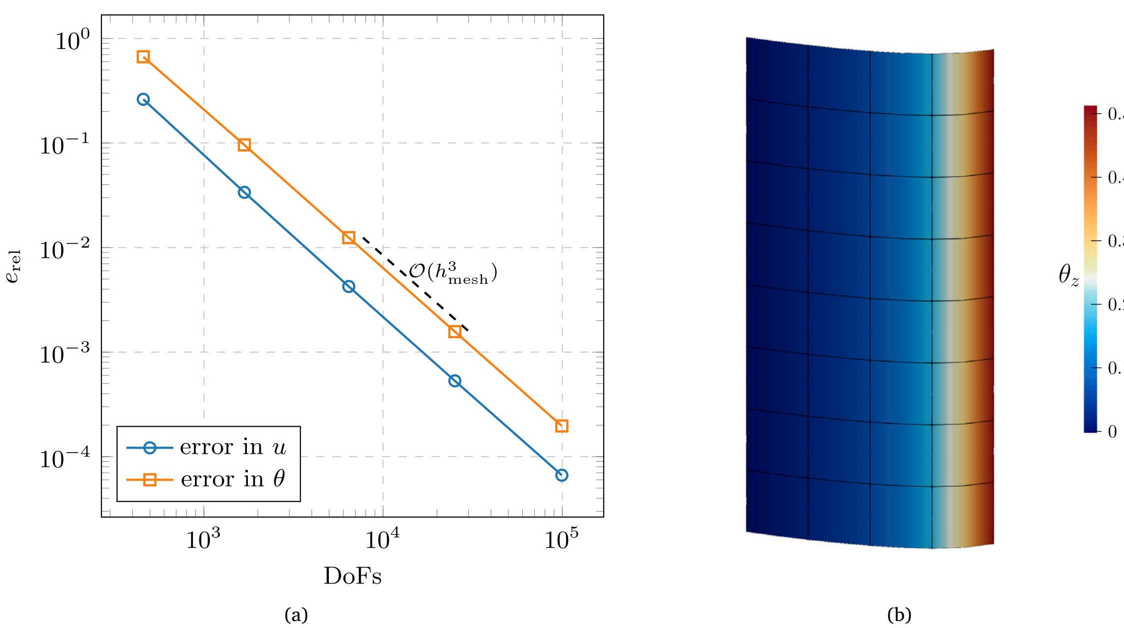

Fig. 4. Convergence of the relative error of the displacement field u_x (round markers) and microrotation field θ_z (square markers) under mesh refinement (a) and deformed domain on the coarsest mesh (b).

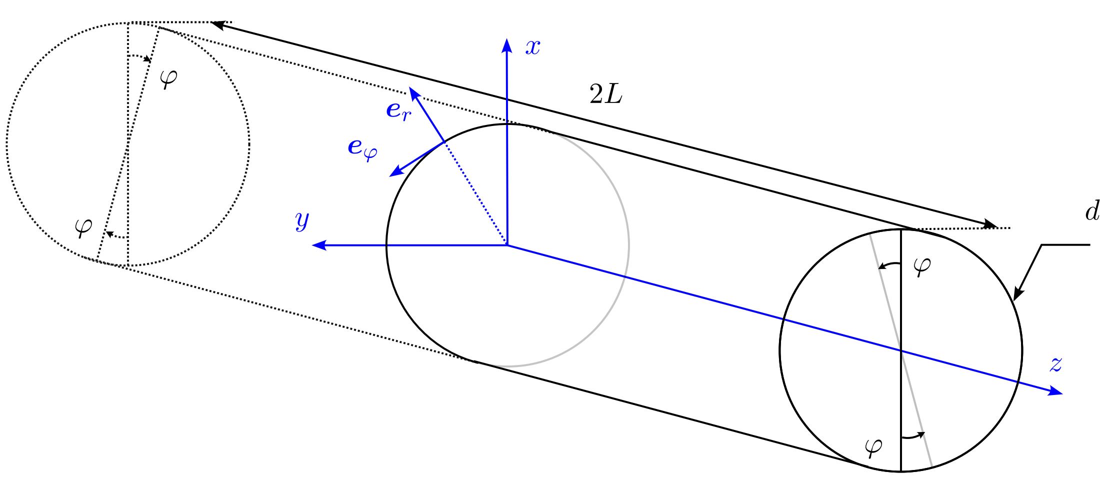

Fig. 5. Torsion of a circular cylinder of length $2L$ under twisting angle of φ. Due to the symmetry in z, the computation is reduced to a cylinder of length L by introducing appropriate symmetry boundary conditions at $z = 0$.

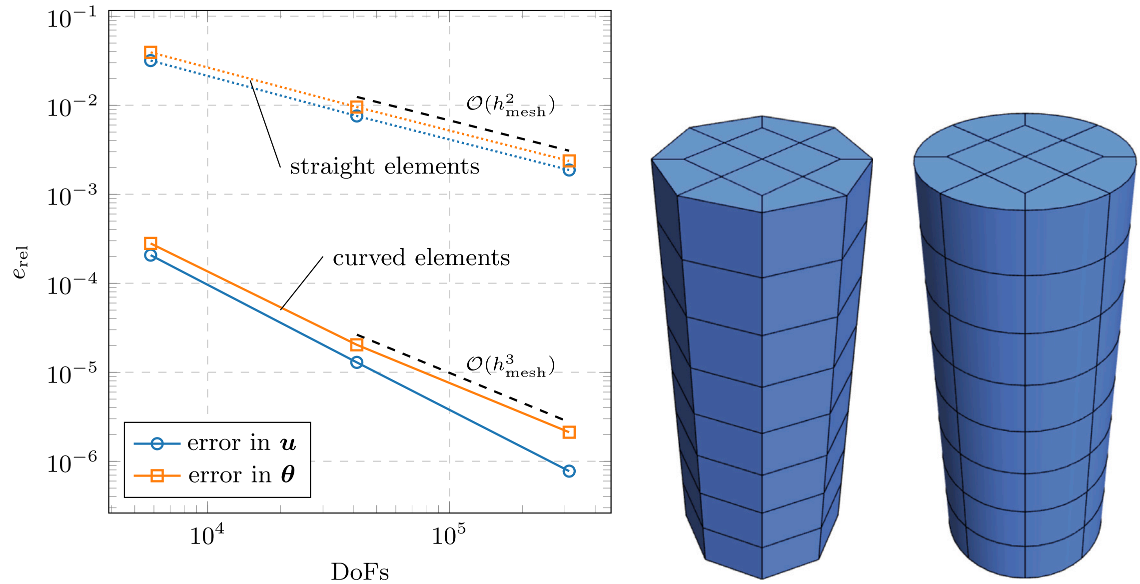

(a) (b) (c)

Fig. 6. Convergence study for the torsion of a circular cylinder with (a) relative L^2 error under uniform mesh refinement for straight and curved elements, (b) straight-edged mesh, (c) curved mesh.

is not directly accessible at the macroscopic scale. When setting up boundary conditions for a torsion test, a key question is as to whether the microrotation should be prescribed directly or left free to respond to its coupling with the displacement field via N. It should be noted that both choices of micro-boundary condition are physically admissible in different contexts. Prescribing the microrotation to follow the macrorotation is appropriate when the microstructure is strongly tied to the macroscopic deformation. Leaving the microrotation free is more appropriate when the substructure can respond independently, as may be the case for metamaterials with macroscopic rotating elements (Eremeyev and Reccia, 2022), where an experimentalist could in principle manipulate the microrotation at the boundary independently of the macroscopic twist.

As shown above, the analytical solution of Gauthier and Jahsman (1975) produces an axial microrotation that coincides with the macrorotation throughout the domain. Prescribing $\theta_z = \varphi$ at the rotating face reproduces this state. Leaving θ_z free with $\mu_{zz} = 0$ on the rotating face as a homogeneous Neumann condition allows the microrotation to respond to the macroscopic twist without being constrained to follow it. Both choices are physically admissible, the question is which one better reflects the physical situation of interest.

In the following, both cases are studied numerically and their effect on the torsional rigidity is compared. Due to an equal but opposed twisting angle φ at both its ends, the computation can be reduced to just one half of the cylinder, introducing appropriate symmetry boundary conditions for both the displacement- and the microrotation fields. At $z = L$, the twisting boundary conditions are

$$u_z = 0, \quad u_x = -\varphi y, \quad u_y = \varphi x, \quad \mu_{xz} = \mu_{yz} = 0 \qquad \text{for } z = L, \tag{33}$$

and for the microrotation θ_z at $z = L$, two distinct boundary conditions are considered: either $\theta_z = \varphi$, or it is left free to follow the macrorotation determined by the micropolar coupling. In the latter case, $\mu_{zz} = 0$ applies. These two different micro-boundary conditions are then compared to analyze their effects. The former choice ($\theta_z = \varphi$) is referred to as "coupled boundary conditions", the latter ($\mu_{zz} = 0$) is referred to as "decoupled boundary conditions". At $z = 0$, the appropriate symmetry boundary conditions are

$$u_x = u_y = 0, \quad \theta_z = 0, \quad \sigma_{zz} = 0, \quad \mu_{xz} = \mu_{yz} = 0 \qquad \text{for } z = 0, \tag{34}$$

where unlike at $z = L$, the boundary condition for the microrotation θ_z is not subject to interpretation but arises directly from the symmetry requirement, which mandates $\theta_z(z) \overset{!}{=} -\theta_z(-z)$ and therefore $\theta_z(z = 0) = 0$.

4.1. Numerical validation

A convergence study for a cylinder with $d = 8\,\text{mm}$ is carried out in the case of prescribed micro- and macrorotation, using parameters fitted for a foam material in Lakes (1983), $\psi = 1.5$, $N = 0.3$, $\mu = 0.6\,\text{MPa}$, and $\ell_t = 3.8\,\text{mm}$. The remaining parameters, which do not enter the analytical solution, are set to $\ell_b = 5\,\text{mm}$ and $\nu = 0.07$, fitted from bending tests of the same material. The domain is discretized with an initial mesh of 96 elements and uniform refinement is applied. Two element types are compared, namely straight-edged and curved quadratic Lagrange elements, shown in Fig. 6(b) and (c), respectively. Straight elements converge suboptimally at $\mathcal{O}(h^2_{mesh})$ while curved elements converge optimally, as shown in Fig. 6(a), where the relative error is computed as defined in (29). On the coarsest curved mesh, the L^2 error in the displacement and microrotation fields is already below 0.03%. In line with (30), the torsional reaction moment is computed in post-processing as

$$M_t = \int_{A|_{z=0}} \left(\sigma_{yz} x - \sigma_{xz} y + \mu_{zz}\right) \mathrm{d}A, \tag{35}$$

where the first two terms represent the contribution from classical tractions and the last term the contribution from couple stresses. On the coarsest curved mesh, the error in M_t is below 0.2%.

4.2. Effect of boundary conditions and polar ratio

In order to investigate the differences between the two discussed boundary condition treatments, the torsional rigidity is analyzed for both in this section. In classical elasticity, the twisting angle φ under an applied torque M_t is determined by $\varphi = \frac{M_t L}{\mu J_t}$, where J_t is the polar moment of inertia (for a cylinder with diameter d it is equal to $\frac{\pi d^4}{32}$). The product $\omega_T = \mu J_t$ is defined as the torsional rigidity, and it will be

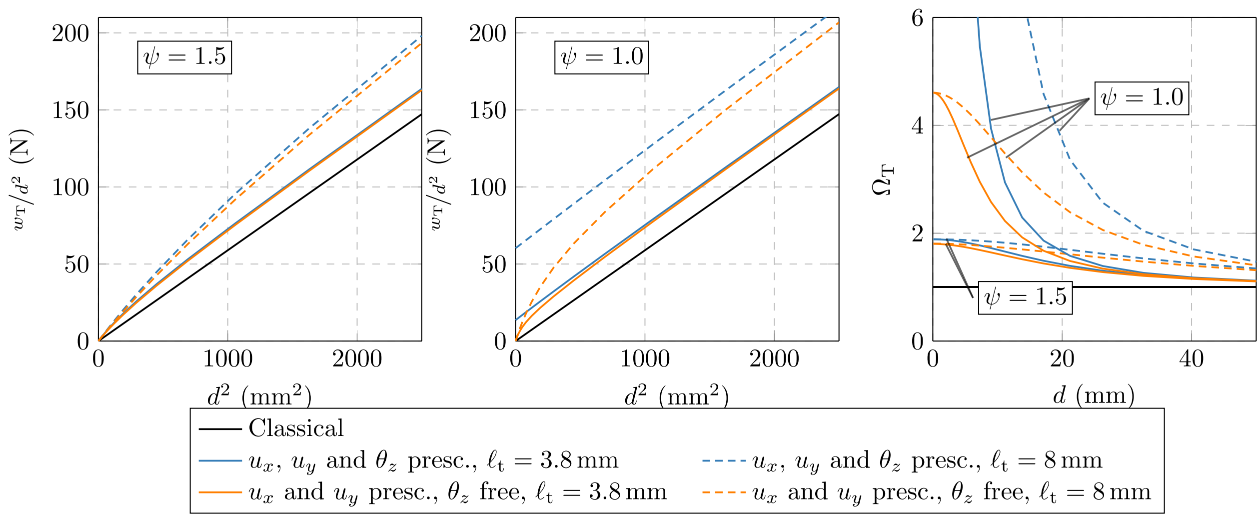

Fig. 7. Torsional rigidity w_T/d^2 and rigidity ratio Ω_T for $\psi = 1.5$ and $\psi = 1.0$. Under coupled boundary conditions, $\psi = 3/2$ is required for bounded Ω_T as $d \to 0$. This restriction is lifted under decoupled boundary conditions.

calculated for the micropolar formulation from the ratio between the applied torque and the resulting twisting angle as

$$w_T = \frac{M_t L}{\varphi}. \tag{36}$$

As the twisting angle φ is prescribed directly in the numerical study, the torque M_t must be calculated during post-processing using (35) where the resulting torsional rigidity can then be compared to the analytical solution provided by Gauthier and Jahsman (1975). This analysis is performed for both sets of boundary conditions and for cylinders with diameters $d \in [0.1\,\text{mm}, 50\,\text{mm}]$. The length-to-radius ratio is held constant at five, such that $L = 5d/2$. In Fig. 7, the torsional rigidity normalized by d^2 is plotted against d^2. In classical elasticity, where $w_T \propto d^4$, this yields a straight line through the origin. Deviations from linearity indicate a micropolar size effect where the torsional rigidity grows faster than d^4 for small diameters, meaning thin cylinders are comparatively stiffer than classical elasticity predicts.

The parameters used are $N = 0.3$, $\mu = 0.6\,\text{MPa}$, $\ell_t = 3.8\,\text{mm}$, $\ell_b = 5\,\text{mm}$ and $\nu = 0.07$, fitted from torsion and bending experiments on a porous solid (Lakes, 1983). Results for $\ell_t = 8\,\text{mm}$ are also shown to illustrate the effect of the characteristic length and two values of the polar ratio are studied, $\psi \in \{1.5, 1.0\}$. The twisting is prescribed as $\varphi = 10°$.

For $\psi = 1.5$, both the coupled and decoupled micro-boundary conditions produce nearly identical results (blue and orange solid lines in left panel of Fig. 7). Both show a pronounced nonclassical size effect at small diameters: the torsional rigidity deviates from the classical d^4 dependence. A larger ℓ_t shifts the onset of this effect toward larger diameters (blue and orange dashed lines in left panel).

For $\psi = 1.0$, the two boundary condition choices produce fundamentally different results. Under coupled micro-boundary conditions, the curves show a constant offset from the classical solution but retain the classical d^4 dependence, with no size effect at small diameters (blue solid line in middle panel). Instead, the torsional rigidity assumes a finite value even as the diameter of the cylinder approaches zero. Under decoupled micro-boundary conditions, however, the pronounced size effect is recovered and the curve departs from linearity at small diameters and approaches zero as $d \to 0$ (orange solid line in middle panel). For larger diameters, the decoupled results approach toward the coupled analytical prediction, with this approach occurring at larger diameters for $\ell_t = 8\,\text{mm}$ than for $\ell_t = 3.8\,\text{mm}$.

The consequences for the torsional rigidity ratio $\Omega_T = w_T/w_{T,\text{cl}}$ are shown on the right panel of Fig. 7. This is the quantity analyzed in Neff (2006), where it is shown that under coupled micro-boundary conditions for this ratio to be bounded as the diameter approaches zero, it is necessary for the polar ratio to be $\psi = 3/2$. The numerical results confirm this, for coupled boundary conditions with $\psi < 3/2$, the ratio grows without bound as the diameter decreases, while for $\psi = 1.5$ it remains bounded. Under decoupled micro-boundary conditions, the ratio remains bounded for all admissible values of ψ. The restriction $\psi = 3/2$ for bounded torsional rigidity is therefore not a property of the constitutive law but a consequence of the micro-boundary condition prescription.

The parameter study in Fig. 8 shows how the three micropolar parameters that appear in the torsion problem independently control the shape of the rigidity ratio curve under decoupled micro-boundary conditions. In Fig. 8(a) for $N = 0.5$ and $\psi = 1.3$, it is shown how the characteristic lengths ℓ_t and $\ell_b = 2\ell_t$ control the onset diameter at which the size effect becomes significant, larger ℓ_t shifts the transition toward larger diameters, while the asymptotic value of Ω_T as $d \to 0$ remains unchanged. In Fig. 8(b) for $\ell_t = 4\,\text{mm}$, $\ell_b = 2\ell_t$ and $\psi = 1.3$, it is shown how the coupling number N controls the magnitude of the plateau at small diameters, a larger N produces a higher asymptotic value of Ω_T. Here it should be noted that the curves for the tested values of N exceed the plot range but remain bounded nonetheless. Finally, in Fig. 8(c) for $N = 0.5$, $\ell_t = 4\,\text{mm}$ and $\ell_b = 2\ell_t$ the effect of the polar ratio ψ is investigated. This parameter controls the rate of transition between the small-diameter plateau and the classical value. All curves remain bounded as $d \to 0$, confirming that the restriction $\psi = 3/2$ is not required under decoupled micro-boundary conditions.

The experimental data of Rueger and Lakes (2019) provides a rare case in which a polar ratio $\psi < 3/2$ is reported for a foam material. The reported material parameters are $\mu = 104\,\text{MPa}$, $N = 0.152$ and $\ell_t = 0.9\,\text{mm}$ and $\psi = 1.493$ (dashed green line in Fig. 9), which produces a much better fit to the torsion size effect data than the fixed value $\psi = 3/2$ (for dotted blue line in Fig. 9). The remaining material parameters are chosen as $\ell_t = 2\ell_b$ and $\nu = 0.3$. Under the coupled micro-boundary conditions of the analytical solution (Gauthier and Jahsman, 1975), any value $\psi < 3/2$ yields an unbounded torsional rigidity ratio as $d \to 0$ (Neff et al., 2010). This is acknowledged in Rueger and Lakes (2019) where it is noted that foam specimens cannot be prepared at arbitrarily small diameters, and thus the inconsistency associated with a divergent ratio is not of practical concern. Still, the present framework resolves this inconsistency. Using decoupled micro-boundary conditions, the polar ratio is identified from the same experimental data by minimizing the deviation between the numerical

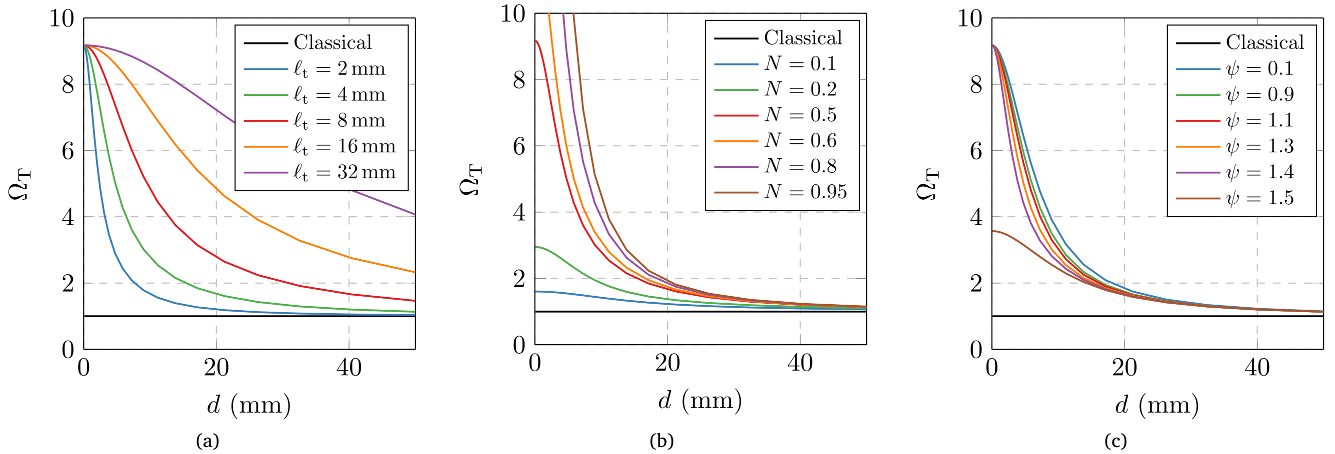

Fig. 8. Torsional rigidity ratio Ω_T under decoupled micro-boundary conditions. (a) ℓ_t controls the onset diameter of the size effect. (b) N controls the magnitude of Ω_T at small diameters. (c) ψ controls the transition rate to the classical value at large diameters.

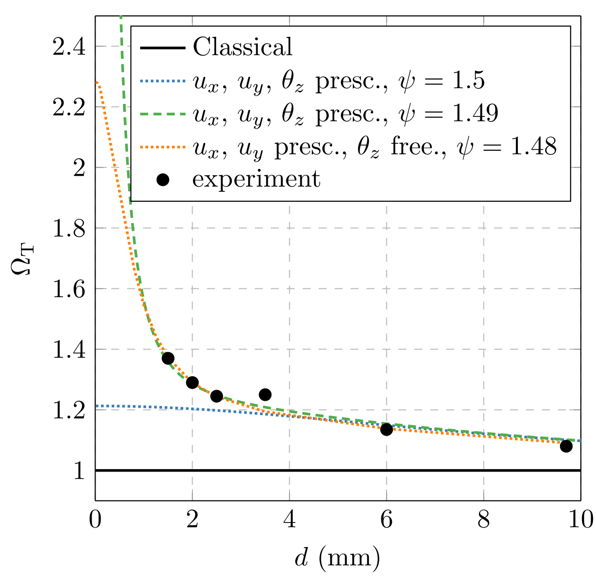

Fig. 9. Torsional rigidity ratio Ω_T for the dense polyurethane foam of experiments from Rueger and Lakes (2019). The numerical solution with decoupled micro-boundary conditions and $\psi = 1.484$ reproduces the experimental data while retaining a bounded rigidity ratio for all $d > 0$.

torsional rigidity and the measured size effects. The resulting fit, shown in Fig. 9, yields $\psi = 1.484$ under decoupled boundary conditions. Crucially, the identified value $\psi = 1.484 < 3/2$ now corresponds to a bounded torsional rigidity ratio Ω_T.

5. Conclusion

In this work, the physical implications of boundary conditions in linearized micropolar elasticity were studied through two boundary value problems, namely the shearing of a long block and the torsion of a circular cylinder. The numerical implementation is made available online, providing a basis for further investigation of boundary condition effects in micropolar elasticity.

An analytical solution for the shearing of a long micropolar block was derived, which treats the displacement and microrotation boundary conditions independently. Unlike the analytical solutions available in the literature, where the deformation shape is predetermined and the micropolar parameters manifest only as a stiffening factor, the present solution allows the deformation shape itself to change with the micropolar parameters and the applied loading. This provides physical interpretations of the micropolar constants that go beyond the classical notion of stiffening: classical forces and micropolar couple stresses drive the displacement and microrotation fields independently when N is small, and the two fields are progressively tied together as $N \to 1$, recovering couple stress theory in the limit. The characteristic bending length ℓ_b controls the stiffness of the microstructure against rotation, and its effect is only visible when couple stresses are present at the boundary.

For the torsion of a circular cylinder, it was shown that the choice of micro-boundary condition has fundamental consequences for the predicted torsional rigidity. When the microrotation is prescribed to coincide with the macrorotation at the rotating face, the analytical solution of Gauthier and Jahsman (1975) is recovered and the torsional rigidity ratio $M_t/M_{t,\mathrm{cl}}$ diverges as $d \to 0$ for $\psi < 3/2$, consistent with the analysis of Neff (2006). When the microrotation is left free at the rotating face, the ratio remains bounded for the full admissible range $\psi \in (0, 3/2)$. From the present results, it is concluded that the restriction $\psi = 3/2$, consistently found when fitting micropolar parameters to torsion experiments via the analytical solution of Gauthier and Jahsman (1975), is a consequence of the boundary condition prescription embedded in that solution rather than a constitutive requirement. This finding expands the admissible parameter space for micropolar models of physical specimens and suggests that the micro-boundary condition prescription deserves explicit attention in both experimental identification and numerical modeling of micropolar solids. As a concrete illustration, the dense polyurethane foam data of Rueger and Lakes (2019), which under the coupled analytical solution required $\psi = 1.493$ and therefore implied an unbounded torsional rigidity ratio as $d \to 0$, is refitted in the present work under decoupled micro-boundary conditions. The identified value $\psi = 1.484$ achieves a comparable fit while yielding a bounded rigidity ratio over the full range of diameters, removing the inconsistency noted in the original study.

CRediT authorship contribution statement

Lucca Schek: Writing – original draft, Visualization, Software, Investigation, Formal analysis, Conceptualization. **Wolfgang H. Müller:** Writing – review & editing, Supervision, Project administration, Funding acquisition, Conceptualization. **Elena N. Vilchevskaya:** Writing – review & editing, Supervision, Conceptualization. **Victor A. Eremeyev:** Writing – review & editing, Supervision, Conceptualization.

Declaration of competing interest

The authors declare that they have no known competing financial interests or personal relationships that could have appeared to influence the work reported in this paper.

Acknowledgment

Funded by the Deutsche Forschungsgemeinschaft (DFG, German Research Foundation) - 525235558.

Appendix A. Eringen formulation

Eringen's original work (Eringen, 1965) introduces the stress and couple stress as

$$\tilde{\sigma}_{ij} = \tilde{\lambda} u_{k,k}\delta_{ij} + \tilde{\mu}\left(u_{i,j} + u_{j,i}\right) + \tilde{\kappa}\left(u_{j,i} - \epsilon_{ijk}\theta_k\right) \tag{37}$$

and

$$\tilde{\mu}_{ij} = \tilde{\alpha}\phi_{k,k}\delta_{ij} + \tilde{\beta}\theta_{i,j} + \tilde{\gamma}\theta_{j,i} \tag{38}$$

where the tilde is introduced to differentiate between the formulation used in this work and the formulation used by Eringen. Even when accounting for the differences in notation for the constants, the expressions for stress and couple stress in Eringen's formulation cannot be directly equated to those in the present work. This is due to Eringen's use of left gradients, meaning the divergences of the stresses in the balance equations (3) and (6) are applied from the left side. In contrast, this work employs right gradients, in accordance with recent solid mechanics literature (see, *e.g.*, Eremeyev et al., 2013; Bertram and Glüge, 2015). Therefore, when comparing the stress and couple stress tensors in recent formulations to those given by Eringen, their transposes must be equated:

$$\sigma_{ij} = \tilde{\sigma}_{ji}, \quad \mu_{ij} = \tilde{\mu}_{ji}, \tag{39}$$

from which expressions for the parameters λ, μ, ν, α, β, γ in (9) and (10) can be derived to express them in terms of the original parameters $\tilde{\lambda}$, $\tilde{\mu}$, $\tilde{\kappa}$, $\tilde{\alpha}$, $\tilde{\beta}$, $\tilde{\gamma}$ used by Eringen. The comparison according to (39) leads to the conversion table in Table 1, from which the parameters in the original formulation can be converted to those used in recent literature (Grbčić et al., 2018), and vice versa.

The Eringen parameterization has the disadvantage that classical and micropolar effects are entangled: a change in $\tilde{\mu}$ or $\tilde{\lambda}$, which one might consider purely classical parameters, also affects the characteristic lengths and coupling number through the conversion in Table 1. The parameterization adopted in this work avoids this by cleanly separating λ and μ from the purely micropolar constants μ_c, α, β, γ.

Appendix B. Analytical solution for the torsion

The analytical solution for the torsion of a circular cylinder from Gauthier and Jahsman (1975), Ghiglione and Forest (2022) is reprinted here as reported in Grbčić et al. (2018). The total torque is (30)

$$M_{\mathrm{T}} = \int_{A|z=L} (r t^{\mathrm{s}}_{\varphi} + m^{\mathrm{s}}_{z})\mathrm{d}A \tag{40}$$

with

$$\begin{aligned} t^{\mathrm{s}}_{\varphi} &= C_1 \mu r + 2\mu_{\mathrm{c}} C_9 I_1(pr), \\ m^{\mathrm{s}}_{z} &= \alpha p C_9 I_0(pr) + 2\beta C_1 \end{aligned} \tag{41}$$

where

$$\begin{aligned} p &= \sqrt{\frac{4\mu_{\mathrm{c}}}{\alpha + 2\beta}}, \\ C_9 &= \frac{M_{\mathrm{t}}}{2\pi\left(\frac{d}{2}\right)^2}\left[\left(\frac{\mu\left(\frac{d}{2}\right)^2}{4\beta} + \frac{3}{2}\right)(\alpha+2\beta)\, p\, I_0\left(\frac{pd}{2}\right) - \left(\frac{\mu\left(\frac{d}{2}\right)^2}{4\beta} + 2\right)\frac{2\beta}{\frac{d}{2}}\, I_1\left(\frac{pd}{2}\right)\right]^{-1}, \\ C_1 &= 2C_9\left(\frac{\alpha+2\beta}{2\beta}\, p\, I_0\left(\frac{pd}{2}\right) - \frac{2}{d}\, I_1\left(\frac{pd}{2}\right)\right), \end{aligned} \tag{42}$$

and where I_0 and I_1 are the modified Bessel functions of the first kind. The resulting displacement and microrotation fields are in cylindrical coordinates

$$\boldsymbol{u} = \begin{pmatrix} 0 \\ \varphi \frac{z}{L} r \\ 0 \end{pmatrix} = \varphi \frac{z}{L} r \boldsymbol{e}_{\varphi}, \qquad \boldsymbol{\theta} = \begin{pmatrix} \phi(r) \\ 0 \\ \varphi \frac{z}{L} \end{pmatrix} = \phi(r)\boldsymbol{e}_r + \varphi \frac{z}{L}\boldsymbol{e}_z, \tag{43}$$

with

$$\begin{aligned} \phi(r) &= -C_1 r/2 + C_9 I_1(pr), \\ \varphi &= C_1 L. \end{aligned} \tag{44}$$

Data availability

Data will be made available on request.

References

Bauer, S., Dettmer, W.G., Perić, D., Schäfer, M., 2012. Micropolar hyperelasticity: constitutive model, consistent linearization and simulation of 3D scale effects. Comput. Mech. 50 (4), 383–396. http://dx.doi.org/10.1007/s00466-012-0679-9.

Bertram, A., Glüge, R., 2015. Solid Mechanics: Theory, Modeling, and Problems. Springer International Publishing, Cham, http://dx.doi.org/10.1007/978-3-319-19566-7.

Beveridge, A., Wheel, M., Nash, D., 2013. The micropolar elastic behaviour of model macroscopically heterogeneous materials. Int. J. Solids Struct. 50 (1), 246–255. http://dx.doi.org/10.1016/j.ijsolstr.2012.09.023.

Cosserat, E., Cosserat, F., 1909. Théorie des Corps déformables. Hermann et Fils, Paris.

Erdelj, S.G., Ibrahimbegović, A., Jelenić, G., 2024. Incompatible-mode geometrically non-linear finite element for micropolar elasticity. Int. J. Solids Struct. 289, 112647. http://dx.doi.org/10.1016/j.ijsolstr.2024.112647.

Erdelj, S.G., Jelenić, G., Ibrahimbegović, A., 2020. Geometrically non-linear 3D finite-element analysis of micropolar continuum. Int. J. Solids Struct. 202, 745–764. http://dx.doi.org/10.1016/j.ijsolstr.2020.05.025.

Eremeyev, V.A., 2019. On non-holonomic boundary conditions within the nonlinear cosserat continuum. In: Abali, B.E., Altenbach, H., dell'Isola, F., Eremeyev, V.A., Öchsner, A. (Eds.), New Achievements in Continuum Mechanics and Thermodynamics. vol. 108, Springer International Publishing, Cham, pp. 93–104. http://dx.doi.org/10.1007/978-3-030-13307-8_7, Series Title.

Eremeyev, V.A., Lebedev, L.P., Altenbach, H., 2013. Foundations of micropolar mechanics. In: SpringerBriefs in Applied Sciences and Technology, Springer Berlin Heidelberg, Berlin, Heidelberg, http://dx.doi.org/10.1007/978-3-642-28353-6.

Eremeyev, V.A., Reccia, E., 2022. On dynamics of elastic networks with rigid junctions within nonlinear micropolar elasticity. Int. J. Multiscale Comput. Eng. 20 (6), 1–11. http://dx.doi.org/10.1615/IntJMultCompEng.2022043259.

Eringen, A.C., 1965. Linear Theory of Micropolar Elasticity. Tech. Rep., Defense Technical Information Center, Fort Belvoir, VA, http://dx.doi.org/10.21236/AD0473723.

Eringen, A.C., 1999. Microcontinuum Field Theories I. Springer New York, New York, NY, http://dx.doi.org/10.1007/978-1-4612-0555-5.

Gauthier, R.D., Jahsman, W.E., 1975. A quest for micropolar elastic constants. J. Appl. Mech. 42 (2), 369–374. http://dx.doi.org/10.1115/1.3423583.

Ghiba, I.-D., Rizzi, G., Madeo, A., Neff, P., 2023. Cosserat micropolar elasticity: classical Eringen vs. dislocation form. J. Mech. Mater. Struct. 18 (1), 93–123. http://dx.doi.org/10.2140/jomms.2023.18.93.

Ghiglione, F., Forest, S., 2022. On the torsion of isotropic elastoplastic Cosserat circular cylinders. J. Micromechanics Mol. Phys. 07 (01), 3–16. http://dx.doi.org/10.1142/s2424913021420078.

Grbčić, S., Ibrahimbegović, A., Jelenić, G., 2018. Variational formulation of micropolar elasticity using 3D hexahedral finite-element interpolation with incompatible modes. Comput. Struct. 205, 1–14. http://dx.doi.org/10.1016/j.compstruc.2018.04.005.

Grbčić, S., Jelenić, G., Ribarić, D., 2019. Quadrilateral 2D linked-interpolation finite elements for micropolar continuum. Acta Mech. Sin. 35 (5), 1001–1020. http://dx.doi.org/10.1007/s10409-019-00870-1.

Ha, C.S., Plesha, M.E., Lakes, R.S., 2016. Chiral three-dimensional isotropic lattices with negative Poisson's ratio. Phys. Status Solidi (B) 253 (7), 1243–1251. http://dx.doi.org/10.1002/pssb.201600055.

Hassanpour, S., Heppler, G.R., 2017. Micropolar elasticity theory: a survey of linear isotropic equations, representative notations, and experimental investigations. Math. Mech. Solids 22 (2), 224–242. http://dx.doi.org/10.1177/1081286515581183.

Lakes, R.S., 1983. Size effects and micromechanics of a porous solid. J. Mater. Sci. 18 (9), 2572–2580. http://dx.doi.org/10.1007/BF00547573.

Lakes, R.S., 1986. Experimental microelasticity of two porous solids. Int. J. Solids Struct. 22 (1), 55–63. http://dx.doi.org/10.1016/0020-7683(86)90103-4.

Lakes, R.S., 1991. Experimental micro mechanics methods for conventional and negative Poisson's ratio cellular solids as cosserat continua. J. Eng. Mater. Technol. 113 (1), 148–155. http://dx.doi.org/10.1115/1.2903371.

Lakes, R.S., 1995. Experimental methods for study of Cosserat elastic solids and other generalized elastic continua. In: Mühlhaus, H. (Ed.), Continuum Models for Materials with Microstructure. Wiley, New York, pp. 1–22.

Lakes, R.S., 2016. Physical meaning of elastic constants in Cosserat, void, and microstretch elasticity. J. Mech. Mater. Struct. 11 (3), 217–229. http://dx.doi.org/10.2140/jomms.2016.11.217.

Müller, W.H., Rickert, W., Vilchevskaya, E.N., 2020. Thence the moment of momentum. ZAMM - J. Appl. Math. Mech. / Z. Angew. Math. Mech. 100 (5), e202000117. http://dx.doi.org/10.1002/zamm.202000117.

Müller, W.H., Vilchevskaya, E.N., 2024. Kontinuumsphysik: Die klassischen Feldtheorien in moderner Darstellung, first ed. Carl Hanser Verlag GmbH & Co. KG, München, http://dx.doi.org/10.3139/9783446479333.

Neff, P., 2006. The Cosserat couple modulus for continuous solids is zero viz the linearized Cauchy-stress tensor is symmetric. ZAMM 86 (11), 892–912. http://dx.doi.org/10.1002/zamm.200510281.

Neff, P., Jeong, J., 2009. A new paradigm: the linear isotropic cosserat model with conformally invariant curvature energy. ZAMM - J. Appl. Math. Mech. / Z. Angew. Math. Mech. 89 (2), 107–122. http://dx.doi.org/10.1002/zamm.200800156.

Neff, P., Jeong, J., Fischle, A., 2010. Stable identification of linear isotropic Cosserat parameters: bounded stiffness in bending and torsion implies conformal invariance of curvature. Acta Mech. 211 (3–4), 237–249. http://dx.doi.org/10.1007/s00707-009-0230-z.

Nowacki, W., 1986. Theory of Asymmetric Elasticity. Polish Scientific Publishers (PWN) & Pergamon Press, Warsaw (Warszawa), Poland & Oxford, UK.

Park, H.C., Lakes, R.S., 1986. Cosserat micromechanics of human bone: Strain redistribution by a hydration sensitive constituent. J. Biomech. 19 (5), 385–397. http://dx.doi.org/10.1016/0021-9290(86)90015-1.

Park, H.C., Lakes, R.S., 1987. Torsion of a micropolar elastic prism of square cross-section. Int. J. Solids Struct. 23 (4), 485–503. http://dx.doi.org/10.1016/0020-7683(87)90013-8.

Pietraszkiewicz, W., Eremeyev, V.A., 2009. On natural strain measures of the non-linear micropolar continuum. Int. J. Solids Struct. 46 (3–4), 774–787. http://dx.doi.org/10.1016/j.ijsolstr.2008.09.027.

Rickert, W., Vilchevskaya, E., Müller, W., 2019. A note on Couette flow of micropolar fluidsaccording to Eringen's theory. Math. Mech. Complex Syst. 7 (1), 25–50. http://dx.doi.org/10.2140/memocs.2019.7.25.

Rueger, Z., Lakes, R.S., 2016. Experimental Cosserat elasticity in open-cell polymer foam. Phil. Mag. 96 (2), 93–111. http://dx.doi.org/10.1080/14786435.2015.1125541.

Rueger, Z., Lakes, R.S., 2019. Experimental study of elastic constants of a dense foam with weak cosserat coupling. J. Elasticity 137 (1), 101–115. http://dx.doi.org/10.1007/s10659-018-09714-8.

Schek, L.N., Massing, F., Vilchevskaya, E.N., Müller, W.H., Eremeyev, V.A., 2026. Deformation measures of micropolar theory in spatial and material description – A review. Contin. Mech. Thermodyn. 38 (2), 16. http://dx.doi.org/10.1007/s00161-025-01438-0.

Schek, L., Müller, W.H., 2026. Numerical and analytical study of elastic parameters in linearized micropolar elasticity. Proc. Appl. Math. Mech. 26 (1), e70058. http://dx.doi.org/10.1002/pamm.70058.

Schöberl, J., 1997. NETGEN An advancing front 2D/3D-mesh generator based on abstract rules. Comput. Vis. Sci. 1 (1), 41–52. http://dx.doi.org/10.1007/s007910050004.

Schöberl, J., 2014. C++11 implementation of finite elements in NGSolve. pp. 1–23, Accepted: 2022-07-29T11:55:15Z.

Sky, A., Hale, J.S., Zilian, A., Bordas, S.P., Neff, P., 2024. Intrinsic mixed-dimensional beam-shell-solid couplings in linear Cosserat continua via tangential differential calculus. Comput. Methods Appl. Mech. Engrg. 432, 117384. http://dx.doi.org/10.1016/j.cma.2024.117384.

Suh, H.S., Sun, W., 2019. An open-source FEniCS implementation of a phase field fracture model for micropolar continua. Int. J. Multiscale Comput. Eng. 17 (6), 639–663. http://dx.doi.org/10.1615/IntJMultCompEng.2020033422.

Tang, P.-Y., 1983. Interpretation of bend strength increase of graphite by the couple-stress theory. Comput. Struct. 16 (1–4), 45–49. http://dx.doi.org/10.1016/0045-7949(83)90146-3.

Thatipelli, K.R., Kalathur, H., S., G., 2026. Size-dependent mechanics in finite cellular lattices: structural and cosserat responses under tension and bending. Int. J. Solids Struct. 326, 113750. http://dx.doi.org/10.1016/j.ijsolstr.2025.113750.

Thiesen, J.L.M., Janczkowski, M.F., Fancello, E.A., 2026. Towards hierarchical micropolar composites: A computational homogenization model of heterogeneous Cosserat media. Int. J. Solids Struct. 332, 113924. http://dx.doi.org/10.1016/j.ijsolstr.2026.113924.

Yang, J.F.C., Lakes, R.S., 1982. Experimental study of micropolar and couple stress elasticity in compact bone in bending. J. Biomech. 15 (2), 91–98. http://dx.doi.org/10.1016/0021-9290(82)90040-9.